RESEARCH ARTICLE

Clean energy of $NiCo_2O_4/MoS_2$ nanocomposites prepared by hydrothermal method

Jie Li*

Material and Chemical Engineering, Zibo Vocational Institute, Zibo, Shandong, China

Received: May 31, 2023; **accepted:** June 28, 2023.

Traditional semiconductor materials such as TiO_2 have a small response range to sunlight, which greatly limits the development and application of photocatalytic technology. In order to enhance the photocatalytic performance of clean energy, the nanocomposite clean energy $NiCo_2O_4/MoS_2$ prepared by hydrothermal method and its performance characterization were investigated. The different semiconductor nanomaterials were compounded with MoS_2, which were modified by the method of constructing heterojunctions to achieve the purpose of enhancing photocatalytic activity and improve the utilization of visible light. Its application properties in the direction of photocatalytic degradation and photolysis of hydrogen from water production were explored. Further, MoS_2 nanorods were synthesized by hydrothermal method, and $NiCo_2O_4$ nanoparticles were loaded on MoS_2 nanorods by *in situ* hydrothermal method to prepare composites $NiCo_2O_4$/CdS. The average hydrogen production rate of the obtained composite material reached 79.27 mmol/h/g in 3 h, and it showed much better photocatalytic stability than MoS_2. Through the close contact between $NiCo_2O_4$ and MoS_2, the photogenerated electrons produced by MoS_2 were effectively separated, which improved the life of photogenerated electrons, making the composite having the advantages of simple preparation method, low production cost, high catalytic activity, and good stability, which provided a new idea for hydrogen production from electrolyzed water.

Keywords: hydrothermal method; clean energy; nanocomposites; energy reduction; photocatalysis; hydrogen evolution reaction.

***Corresponding author:** Jie Li, Material and Chemical Engineering, Zibo Vocational Institute, Zibo 255314, Shandong, China. Email: ljie60501@163.com.

Introduction

As global economic and industrial capabilities develop, the toxic and harmful gases emitted by human production, industries, and daily life continue to increase, which always threatens ecological environmental safety. There are many volatile, flammable, explosive, toxic, and harmful gases such as automobile exhaust, industrial waste gas, and formaldehyde, *etc*. which are always endangering human health, and the leakage of such explosive and toxic gases often occurs in the era of industrialization, which endangers human life. Therefore, continuously improving the level of chemical environmental gas detection, effectively controlling the emission of flammable and explosive gases, and innovating the ability to monitor toxic and harmful gases are important measures to solve ecological and environmental safety issues [1]. These toxic and harmful gases are not only endangering human health but also the culprits of acid rain which causes a big impact to the environmental safety [2]. Therefore, it is of great practical significance to study effective detection methods for such toxic and harmful gases. $NiCo_2O_4/MoS_2$ has the unique two-dimensional structure, high electrical conductivity, large

surface area, and good electrical mobility at room temperature, which determines that it will become a new generation of nanocomposites. Among them, the reduction of $NiCo_2O_4/MoS_2$ has been widely used by researchers in preparation of clean energy because its large surface area and rich functional groups can make up for the shortcomings of metal oxide semiconductors, the gas sensing materials. $NiCo_2O_4/MoS_2$ gas sensors, as new two-dimensional carbon nanomaterials, have high gas-sensitivity properties for toxic and harmful gases at room temperature, which can effectively solve the problem that the nano-based sensor can only work normally at a higher temperature during the gas-sensitive detection process. Currently, the designing and synthesizing nanocomposites with high sensitivity to toxic and harmful gases at room temperature and rapid response recovery rate are worthy of further exploration.

MoS_2 can be self-assembled into a three-dimensional macroscopic columnar aerogel nanocomposite by changing the concentration of reaction raw materials and controlling the reaction temperature and time. The aerogel composite has a channel structure formed by laminating MoS_2 on top of each other, which effectively improves its specific surface area and electrical conductivity. The unique pore structure of the aerogel composite can quickly transmit diffusion molecules during the detection of toxic and harmful gases at room temperature, which makes it full use of the synergy between the two elements to effectively solve the problems of low sensitivity and long response recovery time of a single $NiCo_2O_4/MoS_2$ sensor at room temperature [3]. In recent years, researchers have intensively studied the detection of toxic and harmful gases by $NiCo_2O_4/MoS_2$ nanocomposites, especially after compounding non-metal oxide semiconductors with reduced oxide $NiCo_2O_4/MoS_2$, and their sensitive mechanisms have been explored and studied. A previous study demonstrated that the synthesized $NiCo_2O_4/MoS_2$ nanocomposites showed its sensitivity to 60 ppm MoS_2 of 80% at room temperature with a good gas sensitivity. However, the $NiCo_2O_4/MoS_2$ nanocomposite exhibited poisoning of components and its recovery time was greater than 30 minutes. The gas sensitivity mechanism was also investigated. The results showed that $NiCo_2O_4/MoS_2$ nanocomposites had a large surface area, and $NiCo_2O_4$ nanoparticles were evenly distributed in the reduced-oxidized $NiCo_2O_4/MoS_2$ materials. The synergy between the two elements was used to improve the ability of gas molecules to transport and diffuse. Those results indicated that, although $NiCo_2O_4/MoS_2$ nanocomposite had a good sensitivity mechanism to toxic and harmful gases at room temperature, the lower sensitivity and slower recovery rate of $NiCo_2O_4/MoS_2$ nanocomposites requested in-depth studies [4, 5].

As the promising green material, semiconductor photocatalyst has been widely concerned in many fields such as chemistry, material science, environmental science, *etc*. [6]. Photocatalytic semiconductor materials have many applications such as photocatalytic water to produce hydrogen and photocatalytic reduction of carbon dioxide, which have been considered as renewable clean energy and air purificator. Although solar energy is kind of rich, free, and renewable, the low conversion rate of semiconductor materials and its fast photocarriers recombination directly lead to the low efficiency and poor stability of photocatalytic materials, which limits the practical applications [7]. The photocatalytic efficiency of semiconductors depends not only on nanocomposites' response range, but also the separation and migration characteristics of photocarriers. Recently, the photocatalysis of nanocomposites was effectively improved by adding auxiliary catalysts and coupling with reasonable heterojunctions. In a traditional type-II heterojunction, photogenerated electrons were encouraged to move from the low potential conduction band of one semiconductor to the high potential conduction band of another semiconductor. Concurrently, photogenerated holes on the valence band moved in the opposite direction [8]. Combining semiconductors with

nanocomposites with appropriate band gaps, a promising strategy was provided to improve the photocatalytic activity of nanocomposites by extending the light response range and improving the separation efficiency of photo generated carriers [9]. Theoretically, when the band gap of semiconductor is larger than the potential of photodegradation hydrogen (1.23 eV), it can facilitate the reaction for producing hydrogen. The band gap of MoS_2 is usually 2.4 ev, which is a common semiconductor photocatalytic material [10]. In order to improve the shortcomings of $NiCo_2O_4$ such as fast recombination of photogenerated carriers and photocorrosion, many researchers have been carried out on $NiCo_2O_4$ such as $NiCo_2O_4/TiO_2$, $NiCo_2O_4/BiVO_4$, $NiCo_2O_4/ZnFe_2O_4$, $NiCo_2O_4/ZnS$, $NiCo_2O_4/BiOCl/Ag_2CO_3$, and $ZnO/NiCo_2O_4/CuSbS_2$ [11]. Zinc tungstate ($NiCo_2O_4$) is a wolframite structure and has been widely used in the photodegradation of aquatic hydrogen and the degradation of organic pollutants. However, the band gap of $NiCo_2O_4$ (3.5 ev) limits its response to visible light [12]. The new $NiCo_2O_4/MoS_2$ nanocomposite has obvious photolysis activity for hydrogen production [13]. The remarkable photocatalytic performance is attributed to the effective movement of photogenerated electrons from MoS_2 to $NiCo_2O_4$ through the contact interface, hindering MoS_2 photogenerated carriers' recombination, and prolonging the carrier life [14].

The objectives of this study were to effectively solve the problems of low sensitivity and long response recovery time of $NiCo_2O_4/MoS_2$ gas sensor at room temperature. MoS_2 was employed as the carbon source in this study. It was proposed to synthesize gel 3D macroscopic columnar materials consisting of $NiCo_2O_4/MoS_2$ by combining MoS_2 with different non-metallic oxides such as N-type F_2O_3 and Si_2O_3 with MoS_2, P-type CuO with r GO using freezing and drying techniques. The aerogel nanocomposites were then characterized and tested for component sensitivity, and finally, the growth and gas sensitivity mechanisms were systematically analyzed. The $NiCo_2O_4/MoS_2$ nanocomposites with hollow hexahedral structure were designed and synthesized by hydrothermal method, and their gas-sensitive properties at room temperature were investigated. Through the analysis of the $NiCo_2O_4/MoS_2$ nanocomposites hydrogen production mechanism, structure, optical properties, and electrochemical properties, it would provide a new design scheme of $NiCo_2O_4/MoS_2$ nanocomposites and opened up a new application prospect for more effective use of solar energy.

Materials and Methods

Synthesis of MoS_2 nanorods

Molybdenum disulfide (MoS_2) nanorods were synthesized by using the simple solvothermal method. Briefly, 4.66 g of $Mo(NO_3)_2 \cdot 4H_2O$ and 3.45 g of thiourea were simultaneously dissolved in 70 mL of ethylenediamine and mixed at room temperature for 30 mins before transferred to PCL High Pressure Reactor (Tianjin Fuchen Chemical Reagent Factory, Tianjing, China) at 160°C for 24 hours. When reaching room temperature, it was washed repeatedly with deionized water and anhydrous ethanol and dried in FX101-0 Electric Blast Dryer (Sinopharm Chemical Reagent Co., Ltd, Shanghai, China) at 60°C for 8 hrs.

Preparation of $NiCo_2O_4/MoS_2$ nanocomposites

0.1 g of MoS_2 was dispersed in 30 mL of deionized water by ultrasound. $Mo(NO_3)_2 \cdot 4H_2O$ was dissolved in the above suspension, then 30 mL of $Na_2WO_4 \cdot 4H_2O$ solution was dropped in. After adding NH_4F and stirring for 30 mins, the same process was then conducted as MoS_2 [15]. $NiCo_2O_4/MoS_2$ composited with the mass ratio (wt) of $NiCo_2O_4$ to MoS_2 as 120%, 140%, and 160%, respectively, and were recorded as 1.2-$NiCo_2O_4/MoS_2$, 1.4-$NiCo_2O_4/MoS_2$ and 1.6-$NiCo_2O_4/MoS_2$. Pure $NiCo_2O_4$ was prepared by the same method.

Structure and morphology characterization of $NiCo_2O_4/MoS_2$

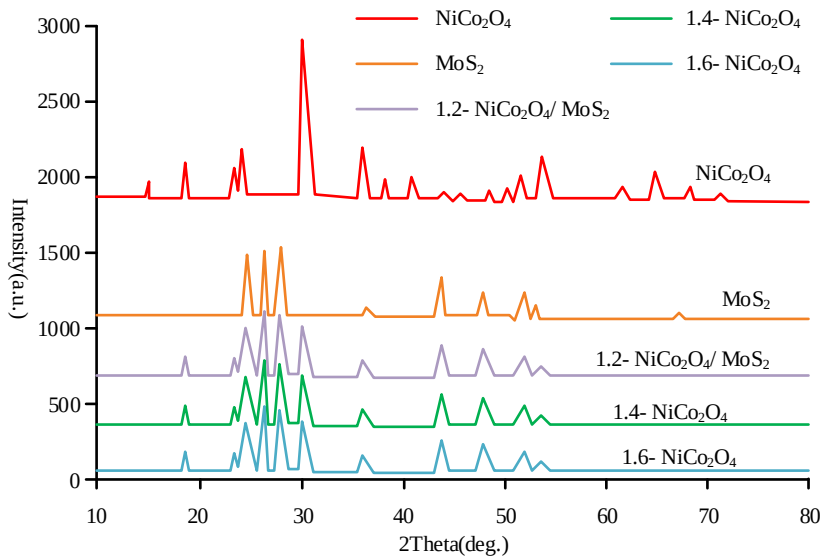

Figure 1. XRD of photocatalytic materials.

The morphologies of MoS_2, $NiCo_2O_4$, and $NiCo_2O_4/MoS_2$ were explored by using Quanta FEG-250 Scanning Electron Microscope (SEM) (FEI, Hillsboro, Oregon, USA) and Hitachi H-800 Transmission Electron Microscope (TEM) (Hitachi, Tokyo, Japan) following manufacturers' instructions. Additional structure analysis was done by using D8-ADVANCE X-ray diffractometer (Bruker, Karlsruhe Germany) following manufacturer's instructions.

Photocatalytic experiment

30 mg of 1.4-$NiCo_2O_4/MoS_2$ composite was mixed with isopropanol (IPA), 1,4-benzoquinone (BQ), and methanol (MeOH) to capture hydroxyl radicals ($\cdot OH$), superoxide radicals ($\cdot O_2^-$), and photogenerated holes (H^+) [16]. 50 mL of Mg (10 mg/L) was added and stirred for 30 mins under dark condition to ensure the adsorption desorption balance between the material and Mg solution [17]. After the dark reaction, the samples were treated by ultrasonic dispersion to make the $NiCo_2O_4/MoS_2$ materials disperse uniformly in the dye solution. Then, a 1 KW Xenon lamp was applied to simulate the visible light irradiation. 3 mL of samples were taken to a colorimetric tube every 20 mins, and the $NiCo_2O_4/MoS_2$ materials in the samples were removed by centrifugation. The UV-Vis spectrophotometer was used to measure the absorbance of the supernatant [18]. The degradation efficiency of the sample to pollutants was calculated by the following formula:

$$D = \left(1 - \frac{C_t}{C_0}\right) \times 100\% \quad (1)$$

where C_0 and C_t were the equilibrium concentrations of Mg solution before and after photocatalytic reaction. Then, the reaction rate constant k was obtained from the first order kinetic equation.

Results and discussion

Structure and morphology characterization of $NiCo_2O_4/MoS_2$

The X-ray diffraction (XRD) patterns of MoS_2, $NiCo_2O_4$, and $NiCo_2O_4/MoS_2$ composites were shown in Figure 1. The results showed that the diffraction peaks of the composites were in accordance with $NiCo_2O_4$ (JCPDS file No.15-0774) and monoclinic MoS_2 (JCPDS file No. 41-1049). $NiCo_2O_4/MoS_2$ composites showed that, when the mass ratio of $NiCo_2O_4$ to MoS_2 increased from

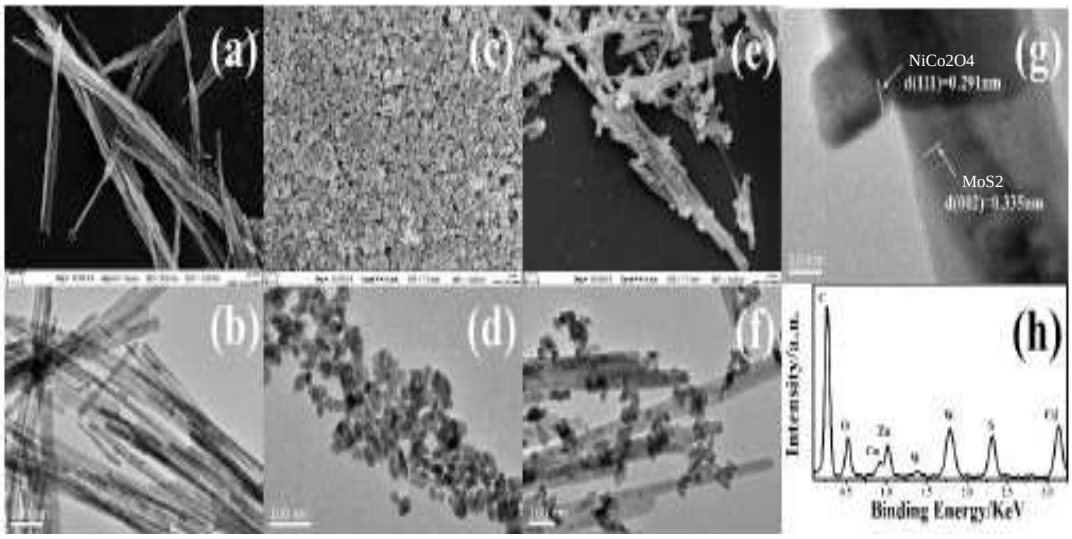

Figure 2. FE-SEM images of MoS_2 (a), TEM images of the pure MoS_2 (b), $NiCo_2O_4$ (c), $NiCo_2O_4$ (d), 1.4-$NiCo_2O_4$/MoS_2 composites (e), 1.4-$NiCo_2O_4$/MoS_2 composites (f), higher magnification TEM image (g), and EDS image (h).

1.2 to 1.6, the crystal structure of the samples had no obvious influence. As mass ratio increased, the diffraction peaks corresponding to 111 and -111 crystal faces of the composites at 30.47˚ and 30.72˚ increased gradually. The crystal diffraction peaks of $NiCo_2O_4$/MoS_2 were clear and well matched, which proved that the material had good crystallinity and two-phase structure without impurities.

The SEM and TEM images of MoS_2, $NiCo_2O_4$, and $NiCo_2O_4$/MoS_2 were shown in Figure 2. MoS_2 was in the shape of a long rod about 1 mm long and 35 nm wide (Figure 2a and 2b), while the $NiCo_2O_4$ had irregular granular morphology (Figure 2c and 2d). When $NiCo_2O_4$ and MoS_2 were combined, $NiCo_2O_4$ nanoparticles were uniformly loaded on MoS_2 rod (Figure 2e and 2f), which proved the intimate contact between $NiCo_2O_4$ and MoS_2. The homogeneous distribution of $NiCo_2O_4$ particles in MoS_2 was not only conducive to photocarriers movement, but also ensured that the active center was exposed to visible light at the same time. Figure 2g showed the high-resolution TEM image of $NiCo_2O_4$/MoS_2 for the further study of its crystal structure. The lattice spacing of 0.335 nm and 0.291 nm corresponded to the 002 crystal surface of MoS_2 and the 111 crystal surface of $NiCo_2O_4$, respectively. The EDS analysis map of $NiCo_2O_4$/MoS_2 composite was shown in Figure 2h, which demonstrated the presence of O, W, Zn, S, and Mo. According to formula 2, 36 kinds of lattice modes could be obtained from the Raman spectra of $NiCo_2O_4$.

$$\Gamma = 8Ag + 10Bg + 8Au + 10Bu \quad (2)$$

In addition to 7 Au and 8 Bu, a total of 15 could be detected by infrared spectrum. Except that 1 Au and 2 Bu were acoustic vibration, only 18 lattice modes could be detected by Raman spectrum including 8 Ag and 10 Bg. Internal modes were caused by the WO bond stretching vibration of WO_6 octahedron and external modems were caused by the motion of WO_6 octahedron to an atom. To further study the structure and composition, the Raman spectra of MoS_2, $NiCo_2O_4$, and $NiCo_2O_4$/MoS_2 composites were studied (Figure 3). The six internal models of $NiCo_2O_4$ were the Ag models of 905 cm^{-1}, 707 cm^{-1}, 544 cm^{-1}, and the Bg models of 781 cm^{-1}, 676 cm^{-1}, 515 cm^{-1}. The diffraction peaks at 342 cm^{-1} and 405 cm^{-1} were caused by the mode deformation of Bg and Ag. The diffraction peaks at 303 cm^{-1} and 606 cm^{-1} were the first-order (1LO) and second-order (2LO) longitudinal optical phonon modes of MoS_2. In the Raman spectrum of 1.4-$NiCo_2O_4$/MoS_2 composite, there were

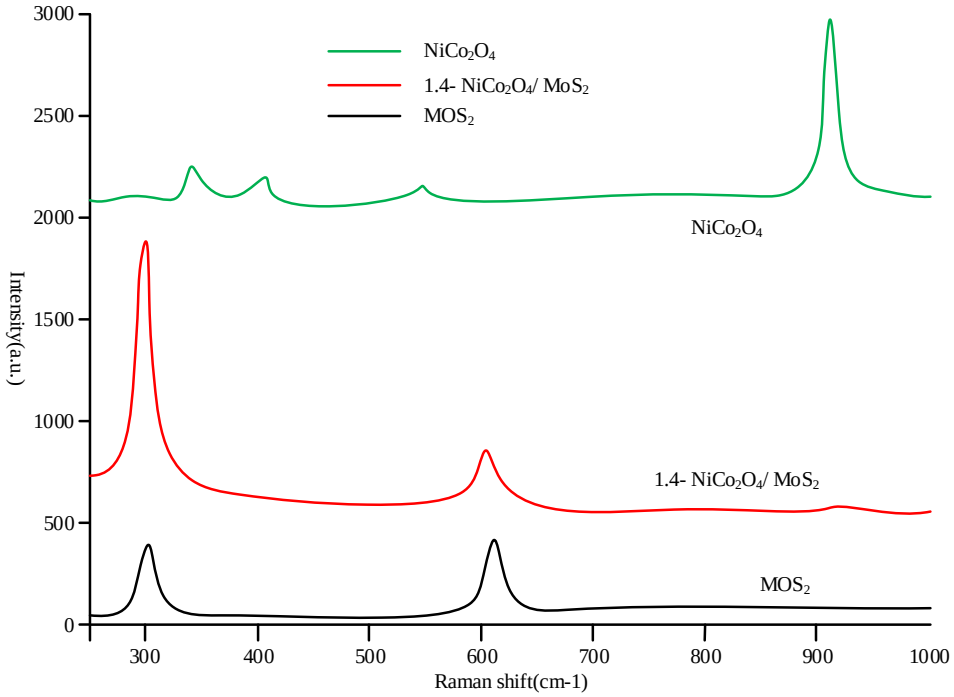

Figure 3. Raman spectra of MoS_2, $NiCo_2O_4$, and 1.4-$NiCo_2O_4$/MoS_2 composites.

three obvious diffraction peaks at 300 cm^{-1}, 600 cm^{-1}, and 905 cm^{-1}, respectively, which indicated that the coupling had no effect on the natural structure of $NiCo_2O_4$ and MoS_2.

Optical properties of $NiCo_2O_4$/MoS_2

In order to analyze the optical absorption characteristics and the recombination rate of photocarriers, the UV-Vis diffuse reflectance and photoluminescence spectra of MoS_2, $NiCo_2O_4$, and $NiCo_2O_4$/MoS_2 composites were measured. MoS_2 showed a wide visible light absorption region due to its narrow band gap, and its absorption band edge was about 525 nm, while the absorption band of $NiCo_2O_4$ was about 325 nm (Figure 4a). Compared with pure MoS_2, the light absorption ability of $NiCo_2O_4$/MoS_2 composite was obviously enhanced. It was shown that $NiCo_2O_4$/MoS_2 composite and MoS_2 had similar optical absorption range and optical response performance in the visible region, which was attributed to the successful coupling between $NiCo_2O_4$ and MoS_2. The PL spectra of MoS_2, $NiCo_2O_4$, and $NiCo_2O_4$/MoS_2 composites at an excitation wavelength of 350 nm were observed. MoS_2 and $NiCo_2O_4$/MoS_2 had similar diffraction peak positions around 530 nm, while $NiCo_2O_4$ had no obvious diffraction peak (Figure 4b). Among them, the lower PL strength of 1.4-$NiCo_2O_4$/MoS_2 composites indicated that the combination of $NiCo_2O_4$ and MoS_2 could better inhibit the recombination of photogenerated carriers in MoS_2. According to the $(ahv)^{1/2}$ correlation curve, the band structure of $NiCo_2O_4$ and MoS_2 was determined from extension line intersection of the linear part and the X axis. α, h and ν represented the absorption coefficient, Planck constant, and optical frequency, respectively. The obtained band gaps of $NiCo_2O_4$ and MoS_2 were approximately 3.5 eV and 2.24 eV (Figure 5a). Furthermore, the VB potential of the semiconductor material could be calculated by formula (3).

$$E_{VB} = X - E^c - 0.5E_g \quad (3)$$

where X was the absolute semiconductor electronegativity. E^c represented free electrons energy in the hydrogen scale (~4.5 eV). E_g

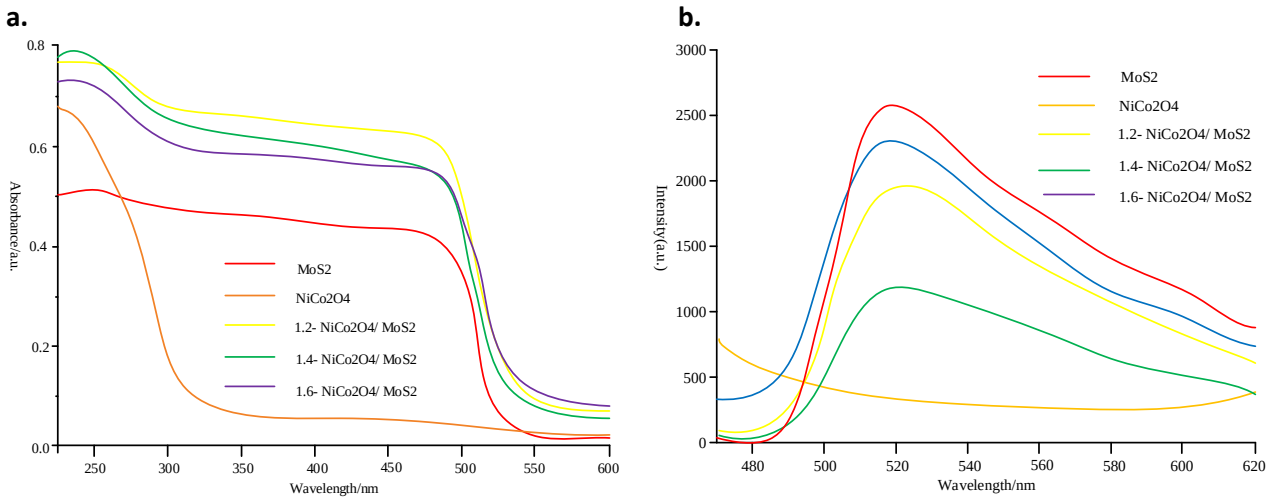

Figure 4. UV-vis diffuse absorption spectra (a) and PL spectra of MoS_2, $NiCo_2O_4$, and $NiCo_2O_4/MoS_2$ composites.

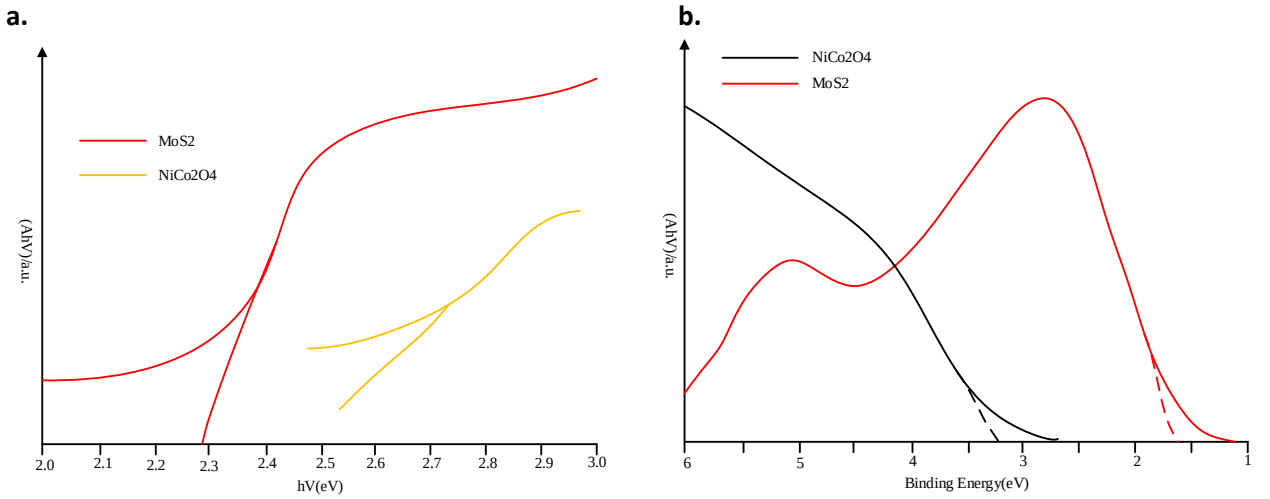

Figure 5. The band gap of $NiCo_2O_4$ and MoS_2 (a) and Valence-band XPS spectra of MoS_2 and $NiCo_2O_4$ (b).

represented the band gap energy. Therefore, the E_{VB} values of $NiCo_2O_4$ and MoS_2 were 3.56 eV and -1.81 eV, respectively. According to formula (4), the E_{CB} values of $NiCo_2O_4$ and MoS_2 were 0.06 eV and -0.43 eV, respectively.

$$E_{CB} = E_{VB} + E_g \quad (4)$$

Visible light did not excite $NiCo_2O_4$., making it impossible to produce $\cdot O_2^-$ (0.08 eV *vs*. normal hydrogen electrode (NHE)) and H_2 (0 eV *vs*. NHE). Therefore, *VB* valence band spectrum of XPS had further determined the occupied electron density and band position of $NiCo_2O_4$ and MoS_2. As shown in Figure 5b, the maximum energy edges of $NiCo_2O_4$ and MoS_2 occupying the highest electronic state density were 2.66 eV and 0.73 eV, respectively. The results showed that the highest occupied electron density of $NiCo_2O_4$ was mainly concentrated in the defect state, rather than the calculated valence band position of the band gap value. The calculated CB edge potentials of $NiCo_2O_4$ and MoS_2 were -0.84 eV and -1.51 eV, which were more negative than the potentials of $O_2/\cdot O_2^-$ and H^+/H_2.

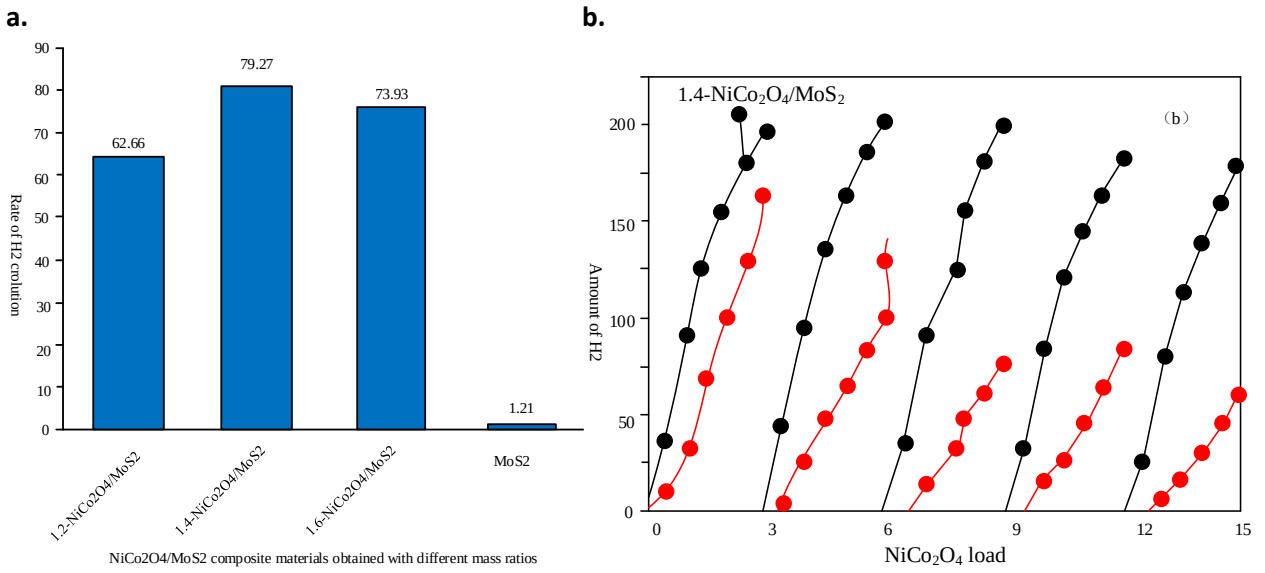

Figure 6. Photocatalytic H_2 evolution rate of MoS_2 and $NiCo_2O_4/MoS_2$ composites (a) and cyclic H_2 evolution curves of 1.4-$NiCo_2O_4/MoS_2$ and MoS_2 (b).

Photoelectrochemical properties of $NiCo_2O_4/MoS_2$

The comparison of the hydrogen production performance of MoS_2 and $NiCo_2O_4/MoS_2$ composites in photolysis was shown in Figure 6a. The Na_2S and Na_2SO_3 were used as sacrificial agents and no precious metal was used as the catalyst. Under visible light, pure MoS_2 underwent slow photolysis of water to produce hydrogen at only 1.21 mmol/h/g. In contrast, as the loading of $NiCo_2O_4$ increased, the hydrogen production activity of $NiCo_2O_4/MoS_2$ composites gradually increased. Among them, 1.4-$NiCo_2O_4/MoS_2$ composites had the highest hydrogen production rate from photolysis water at 79.27 mmol/h/g which was higher than the 1.2-$NiCo_2O_4/MoS_2$ at 62.66 mmol/h/g and the 1.6-$NiCo_2O_4/MoS_2$ at 73.93mmol/h/g. The results showed that the proper $NiCo_2O_4/MoS_2$ could improve its performance by enhancing visible light absorption and the photogenerated carriers' separation. As shown in Figure 6b, five sets of continuous hydrogen production experiments confirmed the stability of 1.4-$NiCo_2O_4/MoS_2$ composites to produce hydrogen from photolysis of water. On the other hand, the decreasing trend of the rate of hydrogen production from photolysis of pure MoS_2 was more obvious, which proved that $NiCo_2O_4/MoS_2$ composites had higher practical applicability. To further prove the photogenerated carrier separation ability and the interfacial charge transport performance, MoS_2, $NiCo_2O_4$, and 1.4-$NiCo_2O_4/MoS_2$ composites were tested for transient photocurrent response and electrochemical impedance spectroscopy. The photocurrent response of 1.4-$NiCo_2O_4/MoS_2$ (62.93 μA/cm^2) was the strongest one, which was better than that of pure MoS_2 (2.92 μA/cm^2) (Figure 7a). Due to the highly efficient synergistic effect between MoS_2 and $NiCo_2O_4$, the separation ability of a single semiconductor material was effectively improved, which reduced the recombination rate of photogenerated electrons and holes and showed a stronger photocurrent response of the composite material. In addition, because the absorption edge around 325 nm caused $NiCo_2O_4$ to respond only to ultraviolet light, $NiCo_2O_4$ did not show the photocurrent response. Compared with the Nyquist diagrams of pure $NiCo_2O_4$ and MoS_2, the diameter of the semicircle of 1.4-$NiCo_2O_4/MoS_2$ was reduced, which proved that the charge transfer resistance of 1.4-

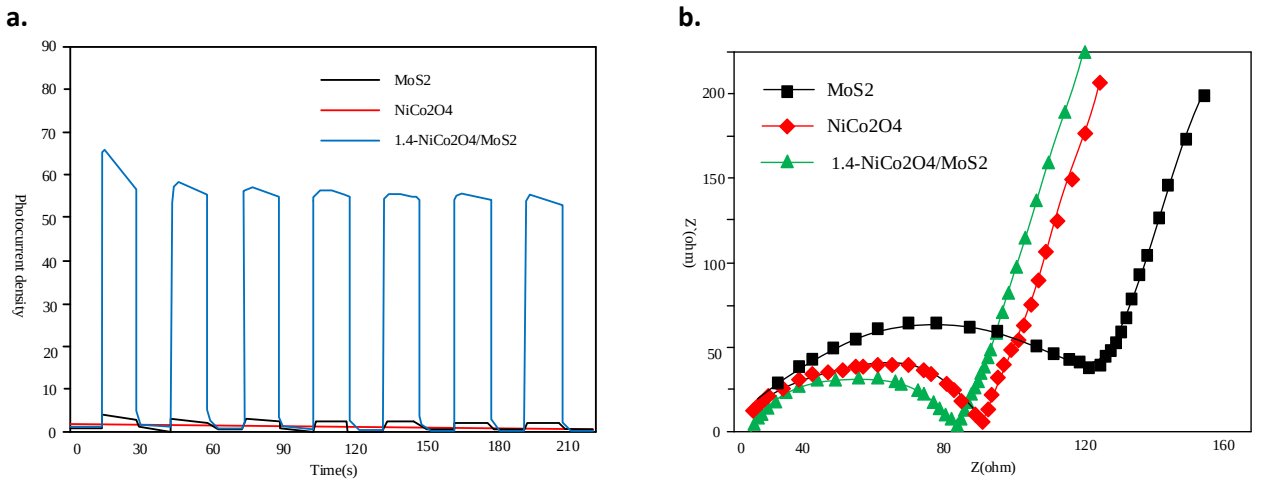

Figure 7. Transient photocurrents response of MoS_2, $NiCo_2O_4$, and 1.4-$NiCo_2O_4$/MoS_2 composites in Na_2SO_4 solution under visible light irradiation (a) and the corresponding EIS of MoS_2 and $NiCo_2O_4$ (b).

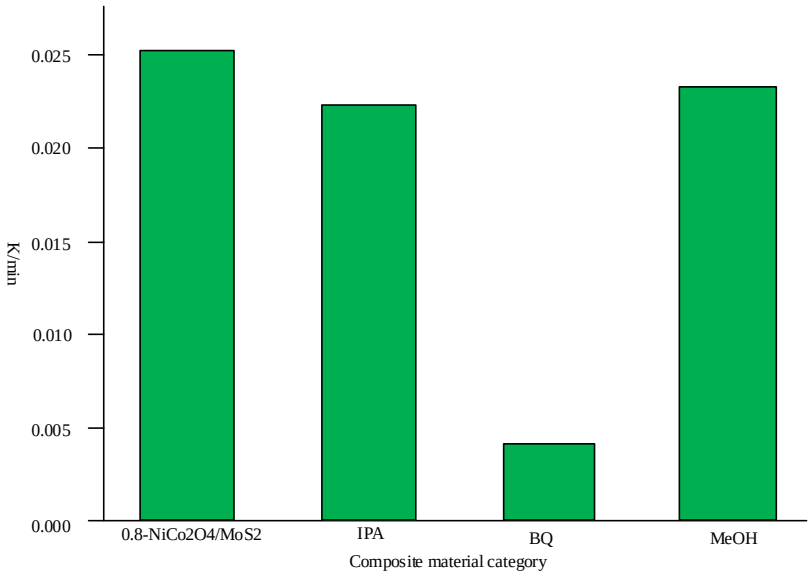

Figure 8. Effects of different scavengers on the degradation of MG in the presence of 1.4-$NiCo_2O_4$/MoS_2 composites under visible-light irradiation.

$NiCo_2O_4$/MoS_2 composites was smaller under visible light irradiation (Figure 7b), which further explained that, due to the effective separation and the rapid transfer effect of composite material, the material had a smaller charge transfer resistance. In order to further study the photocatalytic mechanism of $NiCo_2O_4$/MoS_2 composites, the free radical capture experiments were performed with MG to verify the photogenerated carrier migration pathway. Benzoquinone (BQ), methanol (MeOH), and isopropyl alcohol (IPA) were used to capture superoxide radicals ($\cdot O_2^-$), photogenerated holes (H^+), and hydroxyl radicals ($\cdot OH$). As shown in Figure 8, with the addition of IPA and MeOH, degradation efficiency of 1.4-$NiCo_2O_4$/MoS_2 composites for MG was basically unchanged, and when BQ was added to quench $\cdot O_2^-$, the degradation rate dropped to 65%, which indicated that $\cdot O_2^-$ was main active species. Under visible light, MoS_2 in the heterojunction photocatalytic material was excited by absorbing

photons, and photogenerated electrons in the defect state of MoS_2 were more easily transferred to $NiCo_2O_4$ through intimate contact. After rearrangement, a large number of photogenerated electrons appeared on $NiCo_2O_4$, and photogenerated holes remained on MoS_2, which achieved the purpose of physically separating photogenerated carriers and prevented their recombination. Therefore, photogenerated electrons on $NiCo_2O_4$ reacted with H^+ to generate H_2, and O_2 which adsorbed on $NiCo_2O_4$ active center to generate free radicals. The structure of the $NiCo_2O_4/MoS_2$ composite material maintained the strong reducibility of MoS_2 photogenerated electrons and enhanced the effect of photolysis of water and hydrogen under visible light.

Conclusion

The $NiCo_2O_4/MoS_2$ composites were successfully prepared by *in situ* hydrothermal method in this study. Compared with MoS_2 of 1.21mmol/h/g, the hydrogen production by photolysis in visible light increased significantly by 79.27 mmol/h/g in $NiCo_2O_4/MoS_2$ composites, which remained stable without significant inactivation during the cyclic experiments. From the XPS spectra of $NiCo_2O_4$, MoS_2, and $NiCo_2O_4/MoS_2$ composites, the results showed that MoS_2 was the electron donor in the entire composite system. The free radical capture experiments demonstrated that free radical $\cdot O_2^-$ was the main active species, and the CB potentials of $O_2/\cdot O_2^-$ (0.08 eV *vs*. NHE) and H^+/H_2 was more accurate than that of $NiCo_2O_4$, which illustrated the micro-mechanism of photoinduced carrier migration and separation between $NiCo_2O_4/MoS_2$ composites at the interface. The photocatalytic activity of $NiCo_2O_4/MoS_2$ composites was improved because under visible light, photogenerated electrons on MoS_2 were excited and migrated from MoS_2 to $NiCo_2O_4$, which retained the strong reduction of photogenerated electrons. In this study, a new type of $NiCo_2O_4/MoS_2$ composite material was designed, which provided a new idea for the more efficient use of solar energy for photolysis of aquatic hydrogen and provided a new direction for clarifying the process of photogenerated carrier migration. However, the study only conducted the performance characterization of the composites in laboratory environment, and its small sample size made it difficult to accurately simulate the actual application scenarios. Therefore, additional analysis should be carried out in the subsequent study for the actual application scenarios.

References

1. Tian Q, Wang X, Mao F, Guo X. 2018. Absorption performance of DMSA modified $Fe_3O_4@SiO_2$ core/shell magnetic nanocomposite for Pb^{2+} removal. J Cent South Univ. 25(4):709-718.
2. Xu T, Zhou S, Tao H, Wang W, Zhang K. 2019. Influence of Ag on photocatalytic performance of Ag/ZnO nanosheet photocatalystsag. J Cent South Univ. 26(7):2011-2018.
3. Hümmelgen IA. 2017. Organic electronic solid state device: electrochemistry of material preparation. J Solid State Electrochem. 21(7): 1977–1985.
4. Gurzęda B, Buchwald T, Nocuń M, Bąkowicz A, Krawczyk P. 2017. Graphene material preparation through thermal treatment of graphite oxide electrochemically synthesized in aqueous sulfuric acid. RSC Advances. 7(32):19904-19911.
5. Xie Y, Li Y, Wei G, Liu Q, Mundoor H, Chen Z, *et al*. 2018. Liquid crystal self-assembly of upconversion nanorods enriched by depletion forces for mesostructured material preparation. Nanoscale. 10(9):4218-4227.
6. Zhao Y, Gan Y, Zhang L, Chu Z, Zhang W. 2018. Preparation of ordered mesoporous carbon material based on poly-dopamine and its application in selective enrichment of n-linked glycans. Anal Methods. 10(7):775-782.
7. Panahi S, Es'haghi M. 2018. Preparation and electrochemical characterization of PANI/$MnCo_2O_4$, nanocomposite as supercapacitor electrode material. Can J Chem. 96(5):477-483.
8. Michelina C, Flavia B, Alice SC, Piercarlo M. 2017. $Al_2O_3{\cdot}2SiO_2$ powders synthesized via sol–gel as pure raw material in geopolymer preparation. J Am Ceram Soc. 100(5):1919-1927.
9. Jonna O, Juho AS, Henrikki L. 2017. Preparation of cellulose nanocrystals from lignin-rich reject material for oil emulsification in an aqueous environment. Cellulose. 25(1):293-304.
10. Anna K, Joanna B, Anita TZ, Paulina Z, Marta R. 2017. Structural properties of TiO_2 nanomaterials. J Mol Struct. 1157(5):327-336.
11. Feng X, Wang C, Ding S. 2019. Performance of desulfurization ash for the preparation of grouting fire prevention material. Environ Sci Pollut Res. 26(1):19228–19240.
12. Jun Y, Heng W, Min C, Yang M. 2019. Recent advances in graphene-based nanomaterials: properties, toxicity and

applications in chemistry biology and medicine. Microchimica Acta. 186(6):395.

13. Liu XY, Yang XY, Du H, Wu Y, Zhang J. 2018. Preparation and characterization of a porous silicate material using a CO_2-storage material for CO_2 adsorption. Powder Technology. 333(15):138-152.
14. Liu L, Yang XL, Ye XD, Zhong C. 2017. Preparation and characterization of a photocatalytic antibacterial material: graphene oxide/TiO_2/bacterial cellulose nanocomposite. Carbohydr Polym. 174(15):1078-1086.
15. Li XL, Zhu JF, Fang Y, Lv WJ, Liu Y, Liu H. 2018. Hydrothermal preparation of CoO/Ti_3C_2 composite material for lithium-ion batteries with enhanced electrochemical performance. J Electroanal Chem. 817(15):1-8.
16. Li Y, Xu Y, Fleischer CC, Huang J, Lin R, Yang L, *et al*. 2018. Impact of anti-biofouling surface coatings on the properties of nanomaterials and their biomedical applications. J Mater Chem B. 6(1):9-24.
17. Benjamin L, Alice J, Gillen NS, Wu SJ, Ardemis A. 2019. Directed evolution of the optoelectronic properties of synthetic nanomaterials. Chem Comm. 55(22):3239-3242.
18. Hoo CL, Soon JL, Jungkil K, Kyoung HK, Hong GP. 2019. Unique scattering properties of silicon nanowires embedded with porous segments. ACS Appl Mater Interfaces. 11(23):21094-21099.